



# Large exchange splitting in monolayer graphene magnetized by an antiferromagnet

Yingying Wu<sup>1,7</sup>, Gen Yin<sup>1,7</sup>, Lei Pan<sup>1</sup>, Alexander J. Grutter<sup>1,2</sup>, Quanjun Pan<sup>1</sup>, Albert Lee<sup>1</sup>, Dustin A. Gilbert<sup>1,2,3</sup>, Julie A. Borchers<sup>2</sup>, William Ratcliff II<sup>2</sup>, Ang Li<sup>4</sup>, Xiao-dong Han<sup>4</sup> and Kang L. Wang<sup>1,5,6</sup>✉

**Spin splitting in graphene is required to develop graphene-based multifunctional spintronic devices with low dissipation and long-distance spin transport. Magnetic proximity effects are a promising route to realize exchange splitting in the material, which is otherwise intrinsically non-spin-polarized. Here, we show that monolayer graphene can be magnetized by coupling to an antiferromagnetic thin film of chromium selenide, resulting in an exchange splitting energy as high as 134 meV at 2 K. This exchange splitting is shown through shifts in the quantum Hall plateau and quantum oscillations in the graphene, and its energy can be modulated through field cooling, with the exchange splitting energy increasing with positive field cooling and decreasing with negative field cooling. Our experimental demonstration of magnetism in graphene at low temperatures is supported by measurements of resistivity dependence on temperature and magneto-optic Kerr measurements.**

Spintronic devices, which use the spin of electrons for information storage and logic operations, are widely employed in computing devices in daily use. When information is processed using pure spin current, no net electric current is involved, resulting in a potential solution to the issue of Joule heating in conventional electronic devices. Such devices are of particular interest for low-dissipative device applications<sup>1–4</sup>. Large, nonlocal spin currents have been reported to travel distances of 2 μm to 90 μm at room temperature in monolayer graphene<sup>5–7</sup>, which has been identified as a promising platform for spin-current devices<sup>8</sup>. Although graphene is not inherently spin-polarized, magnetic proximity is known to achieve spin transport in graphene by generating a spin splitting in the band structure. Calculations suggest that this effect can be realized by coupling graphene to ferromagnets such as europium chalcogenides (EuS and EuO)<sup>9–11</sup> and manganese oxide (MnO<sub>2</sub>)<sup>12</sup> or ferrimagnets such as yttrium iron garnet (YIG) and cobalt ferrite (CFO)<sup>13</sup>. It has also been reported experimentally that an exchange coupling can be induced in graphene by an adjacent magnetic insulator of EuS, enabling efficient control of local spin generation and spin modulation in two-dimensional (2D) graphene devices<sup>14</sup>. In particular, nonlocal measurements have identified a magnetic exchange field in graphene on EuS as large as 14 T.

Like ferromagnets and ferrimagnets, antiferromagnets (AFMs) are also magnetically ordered. However, AFMs possess no net magnetization, which eliminates fringing fields and allows information stored in an AFM device to remain insensitive to external magnetic perturbations<sup>15–18</sup>. This stability makes AFM-induced proximity effects highly promising<sup>19</sup>. Theoretical calculations suggest that coupling graphene to the AFM BiFeO<sub>3</sub> may yield an exchange splitting energy of ~70 meV near the Dirac points<sup>20</sup>.

In this Article, we report quantum oscillations in monolayer graphene interfaced with an antiferromagnetic thin film of chromium

selenide (CrSe). At the interface, the π bond formed by the *p* orbitals of carbon is found to overlap sufficiently with the chromium atoms in the CrSe layer to experience a sizeable Hund's-rule exchange coupling. This overlap does not seem to significantly degrade the transport properties of graphene: a Hall mobility of  $1.91 \times 10^5 \text{ cm}^2 \text{ V}^{-1} \text{ s}^{-1}$  is extracted, with clear quantum Hall and Shubnikov–de Haas (SdH) oscillations observed at 2 K. Upon field cooling, changes in the interfacial antiferromagnetic order significantly modify the spin splitting, shifting the spectrum of the SdH oscillations according to the cooling field strength and direction. The proximity-induced magnetization in graphene is also experimentally demonstrated by magneto-optic Kerr effect (MOKE) measurements. The induced spin splitting energy is estimated to be ~134 meV under zero field cooling.

## Magnetic structure of antiferromagnetic CrSe thin films

Bulk Cr<sub>1-*δ*</sub>Se<sub>1+*δ*</sub> is known to have a complex phase diagram, with more than six stable phases in the range  $0.0 \leq \delta \leq 0.05$ . At room temperature, all these phases are pseudo-NiAs CrSe, with the ideal case shown in Fig. 1a, with alternating basal planes of Cr and Se and ordered Cr vacancies in every other Cr layer<sup>21,22</sup>. Neutron scattering studies suggest that most of these structures also possess complex non-collinear antiferromagnetic orders with Néel temperatures ranging from 43 K to 280 K (ref. <sup>23</sup>). Specifically, within each Cr layer of the parent NiAs phase, the magnetic moments are proposed to have an ‘umbrella’-like structure in which the in-plane components of the spins are arranged in a triangular configuration and each layer has a net out-of-plane component that alternates direction along the [001] direction to form an antiferromagnetic crystal with no net magnetization. The Néel temperature (*T*<sub>N</sub>) for the bulk was previously observed to be 280 K (refs. <sup>23,24</sup>).

In addition to a magnetic structure that changes based on stoichiometry and crystal structure, when the NiAs phase of CrSe is

<sup>1</sup>Department of Electrical and Computer Engineering, University of California, Los Angeles, Los Angeles, CA, USA. <sup>2</sup>NIST Center for Neutron Research, National Institute of Standards and Technology, Gaithersburg, MD, USA. <sup>3</sup>Department of Materials Science and Engineering, University of Tennessee, Knoxville, TN, USA. <sup>4</sup>Institute of Microstructure & Properties of Advanced Materials, Beijing University of Technology, Beijing, China. <sup>5</sup>Department of Physics and Astronomy, University of California, Los Angeles, Los Angeles, CA, USA. <sup>6</sup>Department of Materials Science and Engineering, University of California, Los Angeles, Los Angeles, CA, USA. <sup>7</sup>These authors contributed equally: Yingying Wu, Gen Yin. ✉e-mail: [wang@ee.ucla.edu](mailto:wang@ee.ucla.edu)

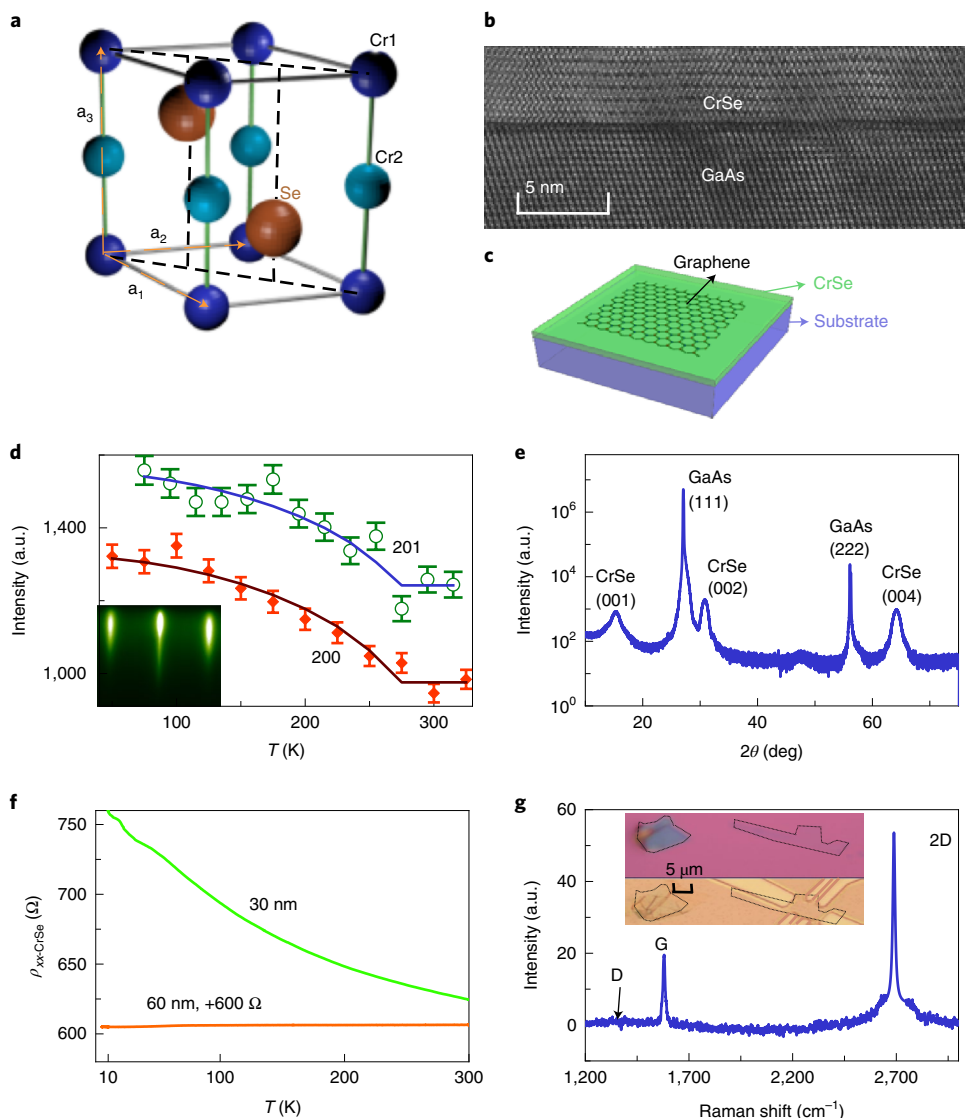


**Fig. 1 | Characterizations of the AFM and graphene/AFM heterostructure.** **a**, Crystal structure of the NiAs-phase CrSe. The three lattice vectors are denoted by  $\mathbf{a}_1$ ,  $\mathbf{a}_2$  and  $\mathbf{a}_3$ . The two sublattices of Cr atoms are denoted by Cr1 and Cr2, respectively. **b**, Transmission electron microscopy side view of the AFM/GaAs, showing the good quality of the AFM. **c**, Schematic of a graphene/AFM heterostructure. **d**, Neutron diffractions of (200)<sub>Mag</sub> and (201)<sub>Mag</sub> Bragg peaks, showing that the Néel temperature for our AFM thin films is close to the reported values. The dots are measured data and the lines are fitting curves. Error bars represent a single standard deviation. The inset shows a reflection high-energy electron diffraction (RHEED) image taken during molecular beam epitaxy growth of CrSe on GaAs. **e**, XRD shows that the AFM is NiAs-type. **f**,  $\rho$ - $T$  curves showing semiconducting behaviour for the AFM with a thickness of 30 nm and metallic behaviour for AFM with a thickness of 60 nm. **g**, Raman spectroscopy shows the signal from monolayer graphene.

grown in thin film, it may exhibit magnetic order and transport behaviour that vary dramatically from those of the bulk due to strain or confinement effects. In this study, CrSe thin films were grown on GaAs (111)B substrates by molecular beam epitaxy. Figure 1b shows a cross-section of the high-quality interface obtained by transmission electron microscopy (TEM). As expected, the line scan indicates a high-quality NiAs-type structure with evidence of ordered Cr vacancies, as can be seen in the dark horizontal stripes. The lattice constants extracted by X-ray diffraction (XRD) are  $a_1 = a_2 = 3.60 \pm 0.01 \text{ \AA}$  and  $a_3 = 5.81 \pm 0.01 \text{ \AA}$ , respectively. These values are in close agreement with reports for NiAs-phase CrSe and Cr<sub>7</sub>Se<sub>8</sub> (refs. <sup>23,25</sup>). Based on the deposition temperature (230°C for the first step and 400°C for the second step) and the relative strengths of the (001) and (002) diffraction peaks, we expect a composition relatively near the stability window of a mixed-phase CrSe/Cr<sub>7</sub>Se<sub>8</sub> (refs. <sup>25–27</sup>).

Although XRD indicates that the films are very near the designed phase, it is critical to directly confirm the antiferromagnetic ordering. We therefore performed neutron diffraction, which revealed strong temperature-dependent (200)<sub>Mag</sub> and (201)<sub>Mag</sub> Bragg peaks, where the 'Mag' subscript indicates that the peaks may be indexed using the rotated and expanded unit cell originally used by Corliss and colleagues<sup>23</sup>. The presence of such a large fully in-plane magnetic diffraction peak requires a large spin component along the growth axis. Furthermore, translating the in-plane contribution of the (200)<sub>Mag</sub> and (201)<sub>Mag</sub> peaks into the structural unit cell indicates a  $[\frac{2}{3}, \frac{2}{3}, 0]$  in-plane propagation vector, suggesting that the expected non-collinear antiferromagnetic order has been preserved. Finally, we note that fitting the temperature-dependent peak intensity of CrSe films on GaAs to a mean-field Brillouin function yields Néel temperatures of  $273 \pm 8 \text{ K}$  and  $270 \pm 7 \text{ K}$ , respectively (unless otherwise noted, error bars and uncertainties represent a single standard

deviation). These results are once again in agreement with the bulk transition temperature of  $\sim 280$  K. Thus, we have shown the presence of high-temperature non-collinear antiferromagnetic order with an out-of-plane spin component.

Despite a magnetic structure that appears to agree well with the bulk, the transport behaviour in a thin-film CrSe strongly depends on the thickness, and can be semiconducting. This is different from the case of bulk, which has always been reported to be metallic<sup>21</sup>. Figure 1f shows the resistivity of 30- and 60-nm CrSe thin films as a function of temperature. The results for the 30-nm thin film suggest a semiconducting behaviour, while the 60-nm film appears to be metallic. The origin of this thickness dependence is unclear at the present stage, but may be related to either vertical quantum confinement in thinner films, or to band bending due to interfacial electrostatics. Regardless of its origin, a 30-nm thickness yields a semiconducting material with an out-of-plane antiferromagnetic order, which is expected to magnetize an adjacent layer of graphene if good proximity can be induced.

### Graphene onto the AFM

Monolayer graphene was first mechanically exfoliated onto a 300-nm-thick  $\text{SiO}_2/\text{Si}$  substrate and then transferred on top of the CrSe thin film (see Supplementary Section A for more details). The Raman spectroscopy shown in Fig. 1g suggests monolayer graphene, and the absence of the D peak indicates a low level of disorder<sup>28,29</sup>.

Quantum oscillations were observed in the graphene/CrSe (30 nm) heterostructure through magneto-transport measurements. As expected, given the antiferromagnetic nature, no ferromagnetic hysteresis was observed. Scanning an out-of-plane magnetic field from  $-9$  T to  $9$  T yields the transport behaviour illustrated in Fig. 2a, where both SdH and quantum Hall oscillations emerge at applied fields exceeding  $\sim 2$  T. To isolate the contribution from the CrSe layer, we also probed the transport behaviour of a control sample composed of a pristine CrSe thin film (30 nm) grown on the insulating GaAs substrate. As shown in Fig. 2b, although the longitudinal resistivity  $\rho_{xx\text{-CrSe}}$  of the control sample is only greater than  $\rho_{xx}$  by about one order of magnitude, the quantum oscillations are completely suppressed, definitively attributing the oscillations in the heterostructure to the Landau levels in the graphene layer. Because the carriers in CrSe are also somewhat involved in the transport,  $\rho_{xy}$  and  $\rho_{xy\text{-CrSe}}$  are comparable, as shown in Fig. 2a,b. The quantum Hall plateaux of the graphene layer are thereby buried in a background associated with the CrSe layer, resulting in a set of ‘kinks’ significantly deviating from the expected multiples of  $\frac{h}{e^2}$ . We therefore extract the Landau level indices and the  $\epsilon_F$  alignment directly from  $\rho_{xx}$  quantum oscillations (Fig. 2a,d), as will be shown later.

More importantly, the quantum oscillation in the graphene can be modulated by field cooling, suggesting a sizeable spin splitting in the graphene layer. As shown in Fig. 2c, the Hall signal can be shifted in opposite directions after positive and negative field coolings. Correspondingly, each quantum Hall ‘kink’ also shifts its position, maintaining its height for all field cooling measurements. The shifts in the SdH minima in  $\rho_{xx}$  as shown in Fig. 2d, are precisely synchronized with the corresponding shifts in the kink locations of  $\rho_{xy}$  as shown in Fig. 2c. The field-cooling-dependent positions of the  $\rho_{xx}$  minima identified by the dashed line at  $n=4$  in Fig. 2d and the  $\rho_{xy}$  kink identified by the arrow in Fig. 2c are plotted together in Fig. 2e to highlight the trend similarity. These transport signatures suggest that the band structure of graphene shifts with respect to  $\epsilon_F$  due to spin splitting, and such spin splitting can be modulated according to the field cooling process.

The spin splitting of the band structure can be further supported by the following three additional experiments. First, without a graphene layer, field cooling hardly influences transport behaviour in the pristine CrSe thin film, as shown in Fig. 2b. Also, pristine monolayer

graphene on a  $\text{SiO}_2/\text{Si}$  substrate cannot respond to field cooling cycles (see Supplementary Section B for details). Finally, the contact resistance is measured to be less than  $600\Omega\mu\text{m}$  (Supplementary Section C), indicating that the  $\pi$  orbital in graphene overlaps sufficiently with the adjacent Cr atoms. These results suggest that the interfacial coupling in the heterostructure is strong, and the field cooling modulation is most likely experienced by the carriers in the graphene layer when hybridized with the Cr electrons in the CrSe layer.

### Exchange splitting in graphene coupled to an AFM

Field cooling is well known as a convenient method to introduce exchange bias in heterostructures formed by a ferromagnet and an AFM<sup>30–33</sup>. For standalone AFM structures, field cooling has also recently been shown to manipulate the Néel vector for certain cases of anisotropy<sup>34</sup>. In particular, uncompensated spins at the surface are expected at the CrSe surface because half of their neighbouring antiparallel moments are missing. They are therefore easier to align with the applied cooling field ( $B_{\text{FC}}$ ) at high temperature, but become pinned on cooling from a temperature far above the Néel temperature, resulting in a net magnetic moment frozen out of plane. The Cr  $d$  orbitals of these frozen moments overlap with the  $p$  orbitals on the adjacent carbon atoms, inducing a spin splitting energy,  $\Delta$  (refs. <sup>11,13,35</sup>). The magnitude of such splitting should be a function of  $B_{\text{FC}}$ .

The position of  $\epsilon_F$  and the spin splitting energy  $\Delta$  can be quantitatively extracted using the Landau fan diagram. In SdH oscillations, each dip of  $\rho_{xx}$  corresponds to a crossing between one Landau level and  $\epsilon_F$ . These dips result in a set of filling factors  $\{\nu\}$  satisfying  $\sigma_{xy} = \nu \frac{e^2}{h}$ , where  $\nu = \pm 4(n \pm \frac{1}{2})$  for  $\epsilon_F \gtrless 0$ , respectively<sup>36,37</sup>. Each quantized  $\sigma_{xy}$  and the corresponding SdH dip can be identified by integer values of  $n=0, 1, 2, \dots$ , counting the Landau levels that can intersect  $\epsilon_F$  due to the band bending near the boundaries. In particular,  $n = \lfloor \frac{\epsilon_F - 1}{\alpha B} \rfloor$  for  $\epsilon_F > 0$  and  $n = \lceil -\frac{\epsilon_F - 1}{\alpha B} \rceil$  for  $\epsilon_F < 0$ , where  $\alpha = 2e\hbar v_F^2$  and  $\lfloor \dots \rfloor$  ( $\lceil \dots \rceil$ ) represents the floor (ceiling) function. Although the Landau level indices  $\{n\}$  are discrete integers, a good approximation is to remove the floor and ceiling brackets to obtain a linear relation between  $n$  and  $\frac{1}{B}$ . As experimentally shown by Zhang and colleagues<sup>36</sup>, for each fixed  $\epsilon_F$  the discrete set of  $\{n\}$  precisely align linearly on a fan of lines  $n = \pm \frac{\epsilon_F^2}{\alpha B} \pm \frac{1}{2}$  with the slopes ( $\beta = \pm \frac{\epsilon_F^2}{\alpha B}$ ) determined purely by the position of  $\epsilon_F$ . Note that the  $\pm \frac{1}{2}$  term comes from the 0th Landau level, where only two of the four degenerate states can intersect  $\epsilon_F$ .

When graphene is magnetized by a sizeable spin splitting energy, the low-energy Hamiltonian of graphene becomes  $H = \hbar v_F \mathbf{k} \cdot \boldsymbol{\sigma} + \frac{\Delta}{2} s_z$ , where  $\boldsymbol{\sigma}$  and  $s$  are the Pauli matrices for sublattices and electron spins, respectively. The valley degree of freedom is not resolved here because the atomic alignment at the interface is difficult to control and the valley splitting should be easily averaged out. The originally degenerate Landau levels now split into two sets, labelled by  $n^\uparrow$  and  $n^\downarrow$  (details of the Landau level index considering the spin splitting term are provided in Supplementary Section D). The filling factor now becomes  $\nu = 2(n^\uparrow + n^\downarrow)$  for  $-\frac{|\Delta|}{2} \leq \epsilon_F \leq \frac{|\Delta|}{2}$ , where  $n^\uparrow = \lceil -(\epsilon_F - \frac{|\Delta|}{2})^2 \frac{1}{\alpha B} \rceil$  and  $n^\downarrow = \lfloor (\epsilon_F + \frac{|\Delta|}{2})^2 \frac{1}{\alpha B} \rfloor$ . When  $\epsilon_F$  is outside the spin splitting region, the filling factor becomes  $\nu = \pm 2(n^\uparrow + n^\downarrow \pm 1)$  for  $\epsilon_F \gtrless \pm \frac{|\Delta|}{2}$ , respectively. Again, the  $\pm 1$  inside the bracket is due to the 0th Landau level. Here,  $n^{\uparrow,\downarrow} = \lceil -(\epsilon_F \pm \frac{|\Delta|}{2})^2 \frac{1}{\alpha B} \rceil$  for  $\epsilon_F < -\frac{|\Delta|}{2}$  and  $n^{\uparrow,\downarrow} = \lfloor (\epsilon_F \mp \frac{|\Delta|}{2})^2 \frac{1}{\alpha B} \rfloor$  for  $\epsilon_F > \frac{|\Delta|}{2}$ . Similar to the spin-degenerate case, by removing the floor and ceiling brackets, we can approximate the slope of the fan diagram using a smooth function:

$$\beta = \begin{cases} -\frac{2}{\alpha} \left( \epsilon_F + \frac{\Delta^2}{4} \right), & \epsilon_F < -\frac{|\Delta|}{2} \\ \frac{2|\Delta|\epsilon_F}{\alpha}, & |\epsilon_F| \leq \frac{|\Delta|}{2} \\ \frac{2}{\alpha} \left( \epsilon_F^2 + \frac{\Delta^2}{4} \right), & \epsilon_F > \frac{|\Delta|}{2} \end{cases} \quad (1)$$

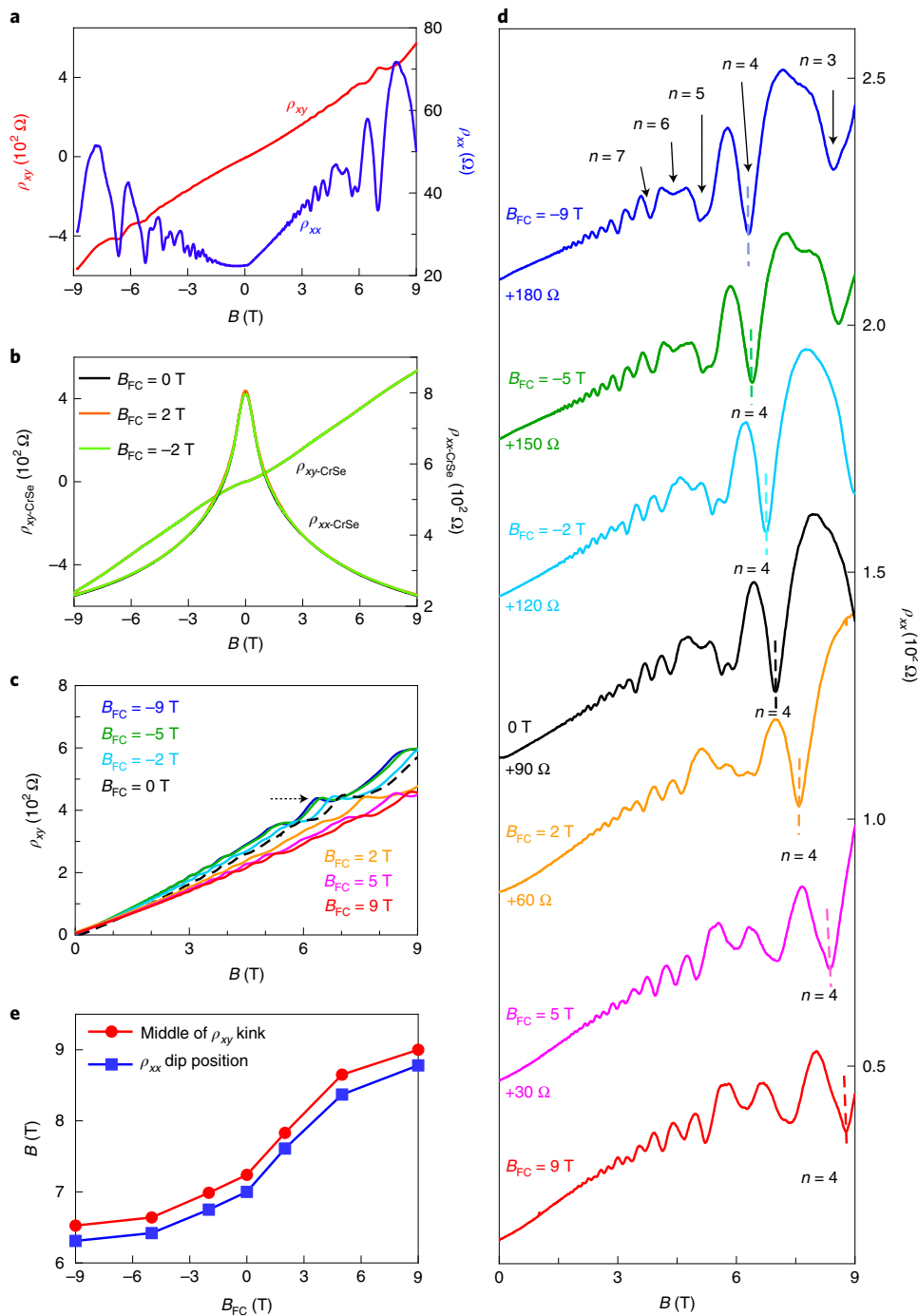


**Fig. 2 | Quantum Hall plateau and quantum oscillations shifted by field cooling.** **a**, Magnetoresistivity (blue curve) and Hall resistivity (red curve) for graphene on CrSe (30 nm) with no external field when cooling. **b**, The Hall resistivity and magnetoresistivity of CrSe (30 nm) at 2 K show little dependence on field cooling.  $B_{FC}$  represents the cooling field, where the subscript 'FC' is short for field cooling. **c**, Quantum Hall plateaux are shifted by field cooling in the heterostructure. The arrow denotes the most pronounced plateau shifted by field cooling. **d**, Quantum oscillations are shifted by field cooling in the heterostructure. The Landau level indices corresponding to each dip are denoted by dark arrows. **e**, For a Landau level index of 4, the red filled circles show the magnetic fields at the middle of the quantum Hall plateaux and the blue squares are for the magnetic fields at the dips of quantum oscillations, as indicated by the dashed lines in **d**.

Note that the value of  $\beta$  now becomes continuous rather than discrete after removing the floor and ceiling brackets. This approximation considers the total Landau fan slope as a simple sum of the up-spin and down-spin slopes, and thereby ignores the sudden changes of the total filling factor due to the Landau level crossings between up- and down-spin states. Detailed discussions of these unsynchronized crossings are provided in Supplementary Section E.

Because  $\Delta$  should be modulated by field cooling as discussed previously, phenomenologically, we assume  $\Delta$  will saturate at large cooling fields:

$$\Delta(B_{FC}) = \Delta_0 + \Delta_1 \tanh(\xi B_{FC}) \quad (2)$$

where  $\Delta_0$  is the splitting energy at  $B_{FC}=0$ ,  $\Delta_1$  denotes the magnitude of the modulation and  $\xi$  is the fitting parameter. Thus, positive and

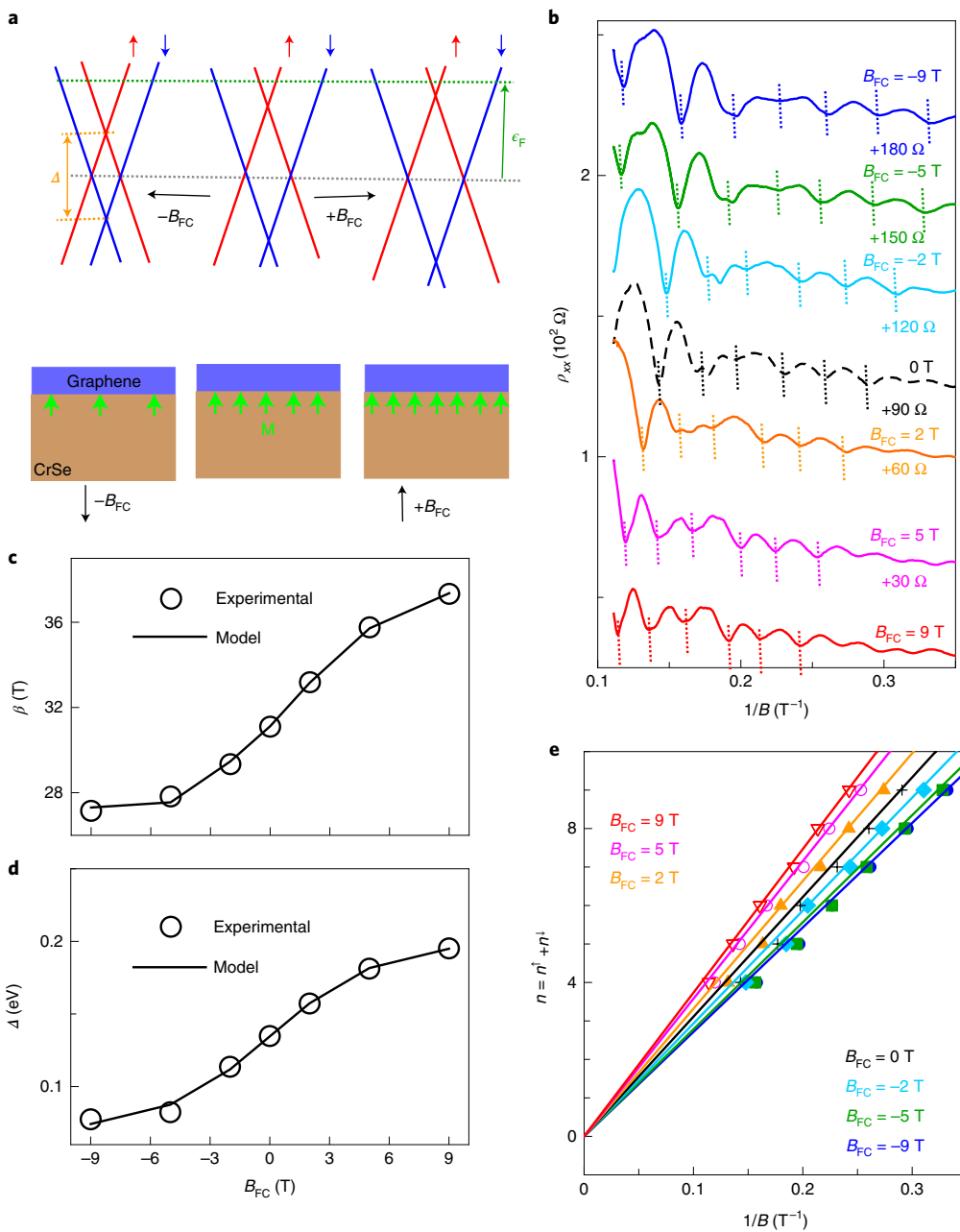


**Fig. 3 | Shifts of quantum Hall plateaux and quantum oscillations modulated by AFM.** **a**, Schematic for graphene coupled to AFM. The red and blue lines represent the linear dispersion near the Dirac points corresponding to the up and down electron spins, respectively. The green arrows in the lower panels represent the remanent magnetization induced at the interface. **b**, The dependence of longitudinal resistivity on the inverse of magnetic fields shows the equally spaced periods of the oscillations. **c,d**, Parameters  $\beta$  (**c**) and  $\Delta$  (**d**) from experiment and fitting using machine learning. **e**, Landau level indices are extracted in the Landau fan diagram for different field coolings, where the dots are the experimental values and the lines are from calculations using parameters given by machine learning.

negative field coolings can shift the up- and down-spin bands in opposite directions, as schematically shown in Fig. 3a, which should modify the slope of the Landau fan diagram accordingly.

To obtain the Landau fan slopes given in equation (2), we replot Fig. 2d in the coordinate of  $\bar{B}$  as shown in Fig. 3b. The dips in  $\rho_{xx}$  are now equally spaced, as expected for the spectrum of graphene. Because each dip of  $\rho_{xx}$  corresponds to an integer change in  $n = n^\uparrow + n^\downarrow$ , the slopes of the Landau fan can therefore be obtained by the period of the SdH dips. These experimental slopes are illustrated by the data points in Fig. 3c. With these values, the parameter set  $X = \{\epsilon_F, \Delta_0, \Delta_1, \xi\}^T$  living in  $\mathbb{R}^4$  becomes over-determined

and therefore can be extracted by searching for the optimal  $X$  that can minimize the overall fitting error. This was achieved by solving a standard machine-learning problem. Converging the average fitting error to less than  $2 \times 10^{-5}$ , the extracted parameters are  $\epsilon_F = 142.4$  meV,  $\Delta_0 = 134.4$  meV,  $\Delta_1 = 65.03$  meV and  $\xi = 0.1834 T^{-1}$ . Details of this learning algorithm and the stability analysis are provided in Supplementary Section F. The Landau fan slopes using these parameters are compared to the fitting targets in Fig. 3c. Note that the position of  $\epsilon_F$  suggests an unintentional doping with a carrier density around  $10^{12} \text{ cm}^{-2}$ , which is probably induced by work function misalignment at the interface. Such a level of unintentional

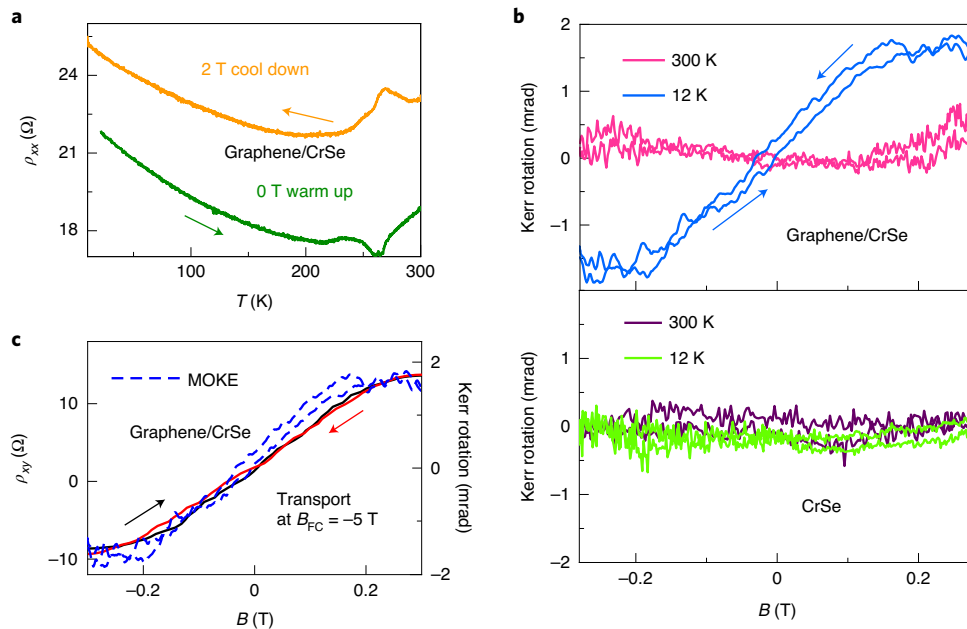


**Fig. 4 | Magnetic phase transition from transport measurements and the MOKE signal.** **a**, Magnetic phase transition revealed by the kink of  $\rho_{xx}$  around 265 K (which is around 8 K lower than the Néel temperature) both at 2 T field cooling and afterwards at 0 T warming up. **b**, MOKE measurements of graphene on CrSe and a control sample. Kerr rotation of graphene on CrSe shows the magnetized graphene at 12 K and no magnetic signal at room temperature. The bottom graph shows the Kerr signal for CrSe on the same substrate. **c**, MOKE data at 12 K compared to the transport data at 2 K of graphene on CrSe.

doping is typical for monolayers of graphene exfoliated on  $\text{SiO}_2$  substrates<sup>38</sup>. Once  $\epsilon_F$  is determined, the values of  $\Delta(B_{\text{FC}})$  can also be directly solved from equation (1) using the experimental values of the slope  $\beta(B_{\text{FC}})$ . These values are then compared to the phenomenological model (equation (2)) in Fig. 3d for self-consistency. The Landau level indices corresponding to each dip in the SdH oscillation can also be determined. Because  $n=0$  has to be satisfied at  $\frac{1}{B} \rightarrow 0$ , there is only one way to assign the integer values of  $n=n^++n^-$  to the SdH dips, as labelled in the previous Fig. 2d. More details are provided in Supplementary Section G. With these values, the experimental Landau fan can then be compared to the one given by the model, as shown in Fig. 3e, where the Landau fan slopes modulated by field cooling can be clearly seen.

The above analysis attributes the slope modulation in the Landau fan diagram only to the exchange splitting energy,  $\Delta$ , whereas the position of  $\epsilon_F$  is assumed to be fixed during field cooling. As discussed above, the position of  $\epsilon_F$  is usually determined by the work function misalignment at the interface. To evaluate this effect, we experimentally extracted the carrier activation energy in a pure CrSe thin film (Supplementary Section H). This energy is estimated to be  $\sim 2$  meV, which is much smaller than  $\Delta$ , so we ignore the field cooling adjustment of  $\epsilon_F$ .

Here, the exchange splitting energy is estimated to be  $\Delta=134.4 \pm 65.03$  meV, where the  $\pm$  amount is adjustable due to field cooling. Such exchange splitting energy should be induced by hybridization between the  $\pi$  orbital of the carbon atoms and the  $d$  orbitals in the Cr atoms, as discussed above. Previous theoretical calculations suggest that this energy can be  $\sim 150$  meV in a graphene/CrI<sub>3</sub> heterostructure<sup>35</sup>. This is within the same order of magnitude as the  $\Delta_0=134.4$  meV extracted in our experiment. Furthermore, spin-orbit coupling (SOC) is also known to impact the transport properties. Such SOC is known to be induced in graphene when interfacing with transition metal dichalcogenides containing heavy elements such as tungsten<sup>39,40</sup>. In these experiments, the SOC energy is extracted from the transport measurements and is estimated to

be within 15 meV. Because Cr atoms are lighter than tungsten, a smaller SOC is expected in our graphene/CrSe heterostructure. The exchange splitting term is greater than the SOC intensity by at least one order of magnitude, so SOC is neglected in our analysis.

The signature of graphene magnetization also appears in the temperature dependence of  $\rho_{xx}$ . Here, we show the measurement of  $\rho_{xx}$  during a cooling-warming cycle for the graphene/CrSe heterostructure spanning a broad range of temperature (10–300 K). An out-of-plane  $B_{\text{FC}}=2$  T was applied during the cooling process, whereas  $B_{\text{FC}}=0$  was used during the warming. As shown in Fig. 4a,  $\rho_{xx}$  presents a peak and a dip for the cooling and the warming processes, respectively. These two features are both present at  $\sim 265$  K, which is in agreement with the Néel temperature ( $\sim 273$  K  $\pm 8$  K) extracted through neutron diffraction, as shown before (Fig. 1d). This suggests that the carrier transport in the heterostructure is indeed influenced by the magnetic order.

### Magnetized graphene in MOKE measurements

The magnetization of graphene in the heterostructure can be probed directly using the polar MOKE effect, with a beam from a linearly polarized laser (633-nm HeNe, power of 50 mW) incident along the surface normal of the graphene/CrSe heterostructure. The detailed set-up is described in Supplementary Section I. During a scan of the out-of-plane magnetic field, any magnetization along  $z$  pinned by the fields should result in a detectable Kerr rotation of the polarization direction. This experiment was carried out both below (12 K) and above (300 K) the estimated Néel temperature. The Kerr rotations for the heterostructure and the pristine CrSe control sample are shown in the top and bottom panels of Fig. 4b, respectively. At 12 K, a sizeable Kerr rotation was observed as a function of the applied magnetic field. The rotation angle presents a super-paramagnetic behaviour for the graphene/CrSe heterostructure, suggesting a detected out-of-plane component of the magnetization when an out-of-plane field is applied. This was not observed in the control CrSe-alone sample at the same temperature. When the temperature

was raised to 300 K, no detectable Kerr rotation was observed in either sample. This suggests that magnetism can indeed be induced in graphene by proximity to CrSe. Furthermore, we also compared the anomalous Hall effect at 2 K (after  $-5$  T field cooling) to the low-temperature MOKE data as shown in Fig. 4c. Both the Hall resistivity and the Kerr rotation angle saturate at around  $\pm 0.25$  T, suggesting a net magnetization induced in the heterostructure.

## Conclusions

We have shown that CrSe thin films with a non-collinear antiferromagnetic spin texture can magnetize monolayer graphene through interface coupling. The exchange splitting energy is identified through field cooling measurements of the graphene/CrSe heterostructure by shifts in the quantum Hall plateau and quantum oscillations. We find an exchange splitting energy of  $\sim 134$  meV, which most likely represents an averaged effect, with atomic details at the interface smeared out. Transport and MOKE measurements also show induced magnetization of the graphene. The modulation of the graphene spectrum is shown to be controllable by the magnetic order at the interface, making it an ideal platform for both exploring quantum interface physics and developing new graphene-based spin-current functionalities. In principle, certain interface arrangements and orientations could possess rich physics that might result in a finite Berry curvature, a Chern insulator or even a  $\mathbb{Z}_2$  invariant<sup>11,20</sup>. Future work could potentially explore systems in which graphene is coupled to insulating AFMs with a variety of crystal symmetries and orientations.

## Methods

**Growth of CrSe.** CrSe thin films were grown in an ultrahigh-vacuum Perkin-Elmer molecular beam epitaxy system. Semi-insulating GaAs [111B] (001) and Al<sub>2</sub>O<sub>3</sub> substrates were cleaned by acetone, with ultrasound, for 10 min before being loaded into the growth chamber. The substrates were then annealed to 580 °C to remove the native oxide under a Se-rich environment. CrSe growth was performed using a two-step growth method. The first step was carried out while the GaAs substrate was maintained at 200 °C with the Cr and Se shutters opened at the same time. After the first step, the substrate temperature was raised to 400 °C and maintained at this temperature to finish the second step growth with the same Cr and Se flux. Epitaxial growth was monitored by an *in situ* RHEED technique, where the digital RHEED images were captured using a KSA400 system built by K-space Associates.

**Neutron diffraction.** Neutron diffraction measurements were performed at the BT4 triple axis diffractometer beamline at the NIST Center for Neutron Research. Measurements were carried out in a temperature range of 10–300 K in a closed-cycle refrigerator. The incident and scattering neutron energy was 14.7 meV ( $\lambda = 2.359$  Å), selected by a pyrolytic graphite (PG) monochromator and analyser crystals with multiple PG filters before and after the sample to eliminate higher-order neutrons. The Soller collimator configuration in downstream order was open-monochromator–40°-sample–40°-analyser–open-detector. Measurements were taken at the reciprocal lattice locations corresponding to the CrSe (002) structural reflection as well as the CrSe (201)<sub>Mag</sub>, (301)<sub>Mag</sub> and (200)<sub>Mag</sub> magnetic reflections. The magnetic reflections were indexed to the bulk magnetic unit cell established by Corliss *et al.*<sup>23</sup>, which is rotated by 30° in the basal plane and has expanded in-plane lattice constants  $a_{\text{Mag}}$  such that  $a_{\text{Mag}} = \sqrt{3} a$ . The magnetic *c* axis was unchanged from the bulk. The in-plane orientation of the CrSe crystal was determined by aligning to in-plane and out-of-plane substrate peaks, specifically along the GaAs [110], [112] and [111] directions. XRD of the GaAs (531) and CrSe (114) peaks reveals in-plane epitaxial alignment between the GaAs [110] and CrSe [110] directions so that the entire reciprocal lattice orientation of CrSe may be determined by locating the GaAs peaks in the neutron diffraction measurement.

**Magneto-transport measurement.** Hall-bar devices with dimensions of  $13\text{ }\mu\text{m} \times 6\text{ }\mu\text{m}$  were fabricated using standard photolithography for the transport measurements. Systematically altering experimental variables such as temperature and magnetic field, in addition to multiple lock-in amplifiers and source meters, enabled comprehensive and high-sensitivity transport measurements in all devices.

## Data availability

The data that support the plots within this paper and other findings of this study are available in figshare with the identifier 10.6084/m9.figshare.12331154 ([https://figshare.com/articles/dataset/source-data-for-Gr-CrSe-paper\\_xlsx/12331154](https://figshare.com/articles/dataset/source-data-for-Gr-CrSe-paper_xlsx/12331154)).

Received: 24 April 2019; Accepted: 9 July 2020;  
Published online: 10 August 2020

## References

1. Han, W., Kawakami, R. K., Gmitra, M. & Fabian, J. Graphene spintronics. *Nat. Nanotechnol.* **9**, 794–807 (2014).
2. Roche, S. & Valenzuela, S. O. Graphene spintronics: puzzling controversies and challenges for spin manipulation. *J. Phys. D* **47**, 094011 (2014).
3. Hill, E. W., Geim, A. K., Novoselov, K., Schedin, F. & Blake, P. Graphene spin valve devices. *IEEE Trans. Magn.* **42**, 2694–2696 (2006).
4. Cho, S., Chen, Y.-F. & Fuhrer, M. S. Gate-tunable graphene spin valve. *Appl. Phys. Lett.* **91**, 123105 (2007).
5. Inglá-Aynés, J., Meijerink, R. J. & Wees, B. J. Eighty-eight percent directional guiding of spin currents with 90-μm relaxation length in bilayer graphene using carrier drift. *Nano Lett.* **16**, 4825–4830 (2016).
6. Drogeler, M. *et al.* Spin lifetimes exceeding 12 ns in graphene nonlocal spin valve devices. *Nano Lett.* **16**, 3533–3539 (2016).
7. Tombros, N., Jozsa, C., Popinciuc, M., Jonkman, H. T. & Van Wees, B. J. Electronic spin transport and spin precession in single graphene layers at room temperature. *Nature* **448**, 571–574 (2007).
8. Stepanov, P. *et al.* Long-distance spin transport through a graphene quantum Hall antiferromagnet. *Nat. Phys.* **14**, 907–911 (2018).
9. Haugen, H., Huertas-Hernando, D. & Brataas, A. Spin transport in proximity-induced ferromagnetic graphene. *Phys. Rev. B* **77**, 115406 (2008).
10. Yang, H.-X. *et al.* Proximity effects induced in graphene by magnetic insulators: first-principles calculations on spin filtering and exchange-splitting gaps. *Phys. Rev. Lett.* **110**, 046603 (2013).
11. Su, S., Barlas, Y., Li, J., Shi, J. & Lake, R. K. Effect of intervalley interaction on band topology of commensurate graphene/EuO heterostructures. *Phys. Rev. B* **95**, 075418 (2017).
12. Gan, L.-Y., Zhang, Q., Guo, C.-S., Schwingenschlögl, U. & Zhao, Y. Two-dimensional MnO<sub>2</sub>/graphene interface: half-metallicity and quantum anomalous Hall state. *J. Phys. Chem. C* **120**, 2119–2125 (2016).
13. Hallal, A., Ibrahim, F., Yang, H., Roche, S. & Chshiev, M. Tailoring magnetic insulator proximity effects in graphene: first-principles calculations. *2D Mater.* **4**, 025074 (2017).
14. Wei, P. *et al.* Strong interfacial exchange field in the graphene/EuS heterostructure. *Nat. Mater.* **15**, 711–716 (2016).
15. Martí, X., Fina, I. & Jungwirth, T. Prospect for antiferromagnetic spintronics. *IEEE Trans. Magn.* **51**, 1–4 (2015).
16. Martí, X. *et al.* Room-temperature antiferromagnetic memory resistor. *Nat. Mater.* **13**, 367–374 (2014).
17. Jungwirth, T., Martí, X., Wadley, P. & Wunderlich, J. Antiferromagnetic spintronics. *Nat. Nanotechnol.* **11**, 231–241 (2016).
18. Moriyama, T. *et al.* Sequential write-read operations in FeRh antiferromagnetic memory. *Appl. Phys. Lett.* **107**, 122403 (2015).
19. Zhou, B. *et al.* Gate-tuned charge-doping and magnetism in graphene/α-RuCl<sub>3</sub> heterostructures. Preprint at <https://arxiv.org/pdf/1811.04838.pdf> (2018).
20. Qiao, Z. *et al.* Quantum anomalous Hall effect in graphene proximity coupled to an antiferromagnetic insulator. *Phys. Rev. Lett.* **112**, 116404 (2014).
21. Polesya, S., Mankovsky, S., Benea, D., Ebert, H. & Bensch, W. Finite-temperature magnetism of CrTe and CrSe. *J. Phys. Condens. Matter* **22**, 156002 (2010).
22. Ivanova, V., Abdinov, D. S. & Aliev, G. On some characteristics of chromium selenides. *Phys. Status Solidi B* **24**, K145–K147 (1967).
23. Corliss, L., Elliott, N., Hastings, J. & Sass, R. Magnetic structure of chromium selenide. *Phys. Rev.* **122**, 1402 (1961).
24. Makovetskii, G. & Shakhlevich, G. Magnetic properties of the CrS<sub>1-x</sub>Se<sub>x</sub> system. *Phys. Status Solidi. A* **47**, 219–222 (1978).
25. Katsuyama, S., Ueda, Y. & Kosuge, K. Phase diagram and order-disorder transition of vacancies in the Cr<sub>1-x</sub>Se and Fe<sub>1-x</sub>Se systems. *Mater. Res. Bull.* **25**, 913–922 (1990).
26. Yan, J. *et al.* Anomalous Hall effect in two-dimensional non-collinear antiferromagnetic semiconductor Cr<sub>0.68</sub>Se. *Appl. Phys. Lett.* **111**, 022401 (2017).
27. Hayashi, A. *et al.* Cation distribution in (M', M)<sub>3</sub>Se<sub>4</sub>; II. (V,Ti)<sub>3</sub>Se<sub>4</sub> and (Cr,V)<sub>3</sub>Se<sub>4</sub>. *J. Solid State Chem.* **71**, 237–243 (1987).
28. Graf, D. *et al.* Spatially resolved Raman spectroscopy of single-and few-layer graphene. *Nano Lett.* **7**, 238–242 (2007).
29. Ferrari, A. C. *et al.* Raman spectrum of graphene and graphene layers. *Phys. Rev. Lett.* **97**, 187401 (2006).
30. Zhu, W., Seve, L., Sears, R., Sinkovic, B. & Parkin, S. Field cooling induced changes in the antiferromagnetic structure of NiO films. *Phys. Rev. Lett.* **86**, 5389 (2001).
31. Ambrose, T. & Chien, C. Dependence of exchange field and coercivity on cooling field in NiFe/CoO bilayers. *J. Appl. Phys.* **83**, 7222–7224 (1998).
32. Koon, N. Calculations of exchange bias in thin films with ferromagnetic/antiferromagnetic interfaces. *Phys. Rev. Lett.* **78**, 4865 (1997).

33. Hoffmann, A. Symmetry driven irreversibilities at ferromagnetic-antiferromagnetic interfaces. *Phys. Rev. Lett.* **93**, 097203 (2004).
34. Kriegner, D. et al. Multiple-stable anisotropic magnetoresistance memory in antiferromagnetic MnTe. *Nat. Commun.* **7**, 11623 (2016).
35. Zhang, J. et al. Strong magnetization and Chern insulators in compressed graphene/CrI<sub>3</sub> van der Waals heterostructures. *Phys. Rev. B* **97**, 085401 (2018).
36. Zhang, Y., Tan, Y.-W., Stormer, H. L. & Kim, P. Experimental observation of the quantum Hall effect and Berry's phase in graphene. *Nature* **438**, 201–204 (2005).
37. Gusynin, V. & Sharapov, S. Unconventional integer quantum Hall effect in graphene. *Phys. Rev. Lett.* **95**, 146801 (2005).
38. Tan, Y.-W. et al. Measurement of scattering rate and minimum conductivity in graphene. *Phys. Rev. Lett.* **99**, 246803 (2007).
39. Wang, Z. et al. Origin and magnitude of 'designer' spin-orbit interaction in graphene on semiconducting transition metal dichalcogenides. *Phys. Rev. X* **6**, 041020 (2016).
40. Wang, Z. et al. Strong interface-induced spin-orbit interaction in graphene on WS<sub>2</sub>. *Nat. Commun.* **6**, 8339 (2015).

## Acknowledgements

The transport measurement and theoretical modelling in this work were supported by Spins and Heat in Nanoscale Electronic Systems (SHINES), an Energy Frontier Research Center funded by the US Department of Energy (DOE), Office of Science, Basic Energy Sciences (BES) under award #SC0012670. We are also grateful for support from the National Science Foundation (NSF) (DMR-1411085 and DMR-1810163) and the ARO programme (contract no. W911NF-15-1-10561). Research was performed in part at the NIST Center for Nanoscale Science and Technology. This work used the Extreme Science and Engineering Discovery Environment (XSEDE), which is supported by NSF grant no. OCI-1053575. Specifically, it used the Bridges system (supported by NSF award no.

ACI-1445606) at the Pittsburgh Supercomputing Center (PSC). Certain commercial equipment, instruments or materials are identified in this paper to foster understanding. Such identification does not imply recommendation or endorsement by the National Institute of Standards and Technology, nor does it imply that the materials or equipment identified are necessarily the best available for the purpose.

## Author contributions

Y.W., G.Y. and K.L.W. conceived and designed the experiment. K.L.W. supervised the work. L.P. grew the CrSe samples. Y.W. carried out the fabrication and transport measurements. G.Y. and A. Lee performed the theoretical calculations and machine learning. A.J.G., D.A.G., J.A.B. and W.R.II performed and analysed the X-ray spectroscopy and neutron diffraction. Q.P. performed the MOKE measurements. A. Li and X. Han performed the transmission electron microscopy measurement. All authors contributed to the measurement and analyses. Y.W., G.Y., A.J.G. and K.L.W. wrote the manuscript with contributions from all the authors.

## Competing interests

The authors declare no competing interests.

## Additional information

**Supplementary information** is available for this paper at <https://doi.org/10.1038/s41928-020-0458-0>.

**Correspondence and requests for materials** should be addressed to K.L.W.

**Reprints and permissions information** is available at [www.nature.com/reprints](http://www.nature.com/reprints).

**Publisher's note** Springer Nature remains neutral with regard to jurisdictional claims in published maps and institutional affiliations.

© The Author(s), under exclusive licence to Springer Nature Limited 2020